Comprehensive model for evaluating voltage losses and performance improvements in thin-film photovoltaic devices

Marco Nardone,[1,*] Sakshi Gupta,[1] Eva Mulloy,[1] Steve Johnston,[2] Eric Colegrove,[2] Joel N. Duenow,[2] Brian Good,[2] Craig L. Perkins,[2] Darius Kuciauskas,[2] and Matthew O. Reese[2]

[1] *Department of Physics and Astronomy, Bowling Green State University, Bowling Green, Ohio 43403, USA*

[2] *National Renewable Energy Laboratory, 15013 Denver West Pkwy, Golden, Colorado 80401, USA*

(Received 6 July 2024; revised 3 December 2024; accepted 10 February 2025; published 10 March 2025)

Progress of state-of-the-art and next-generation thin-film photovoltaic devices is often stymied by open-circuit voltage (V_{oc}) that is significantly lower than theoretical and practical limits. Yet, effectively diagnosing the primary sources of voltage loss remains challenging. Herein, a sequence of device-level characterization techniques and simulations are employed to identify and rank loss mechanisms. For the research-based Cd(Se, Te) device under study, most of the loss was at the front semiconductor heterointerface due to a clifflike conduction-band offset that lowered the recombination activation energy. Additional losses due to band tails were quantified by photoluminescence analysis. The latter provided the absorption coefficient and activation energy reduction associated with band tails as inputs to device models. Simulations showed that alleviating front-interface issues would improve V_{oc}, but it would then be limited by bulk recombination. Further improvement of the bulk would then lead to back-contact limitations. Reducing band tails is beneficial in any circumstance. This analysis provides guidance for reaching toward the radiative V_{oc} limit.

DOI: 10.1103/PhysRevApplied.23.034019

I. INTRODUCTION

Thin-film photovoltaic (TFPV) and emerging devices continue to make advances in power conversion efficiency (η) [1]. A key challenge moving forward is overcoming open-circuit voltage (V_{oc}) deficits exhibited by technologies based on perovskite [2], kesterite [3], Cu(In, Ge)Se_2 [4], and CdTe [5,6]. Therefore, effective approaches for diagnosing the dominant causes of voltage loss are imperative. In this work, an approach is demonstrated that combines multiple device-level characterization techniques and device simulation to distinguish and rank V_{oc} loss mechanisms. In particular, current density versus voltage at various temperatures and light intensities (JVTi), quantum efficiency (QE), photoluminescence (PL), and time-resolved photoluminescence (TRPL) were measured and modeled to determine V_{oc} losses associated with bulk recombination (radiative and nonradiative), front interface, back interface, and band tails. We also utilized thermomechanical cleaving to access the SnO_2/Cd(Se, Te) interface for x-ray photoelectron spectroscopy (XPS), ultraviolet photoelectron spectroscopy (UPS), and low-energy inverse photoemission spectroscopy (LEIPS), to determine band alignments. Results are compared with device modeling as a means of independently assessing band positions. Other measurements, including capacitance-voltage (C-V) and secondary ion mass spectroscopy (SIMS), provided complementary electronic and chemical information.

As a case study, we considered Cd(Se, Te) devices, which are currently the thin-film market leader with continued growth trajectory [5]. The thermodynamic (Shockley-Queisser, SQ) limit is $V_{oc} = 1.122$ V for a band gap of 1.4 eV, and $V_{oc} = 1.215$ V for a band gap of 1.5 eV [7]. Yet, record V_{oc} of approximately 0.9 V has persisted for a decade in polycrystalline CdTe-based devices (band gap of 1.5 eV) [5]. The current record laboratory efficiency is $\eta = 23.1\%$ [1]. Increasing V_{oc} close to 1 V is critical for achieving $\eta = 25\%$ [8]. Strategies to achieve that goal should be guided by device-specific limitations and understanding where the greatest losses occur. Possible issues include bulk nonradiative and interface recombination, interface band alignments, doping, carrier mobility, and band tails. Also important are optimizing carrier selective contacts [6,9,10], and reducing spatial nonuniformities [11,12]. Advances beyond $V_{oc} = 1$ V will likely require clever optical management. Herein, V_{oc} loss evaluation is conducted to identify pathways for improvement of a research-based device that has moderate $\eta = 15.9\%$ and $V_{oc} = 744$ mV. The key question is where to focus improvement efforts.

*Contact author: marcon@bgsu.edu

The adoption of the ternary alloy Cd(Se, Te) for CdTe-based devices has led to marked improvements in performance but it has also increased the probability of disorder-induced deleterious effects. Anion disorder between Se and Te sites, fluctuating band gaps, and the propensity for dopant compensation can result in significant band tails. It has been shown that band tails with characteristic decay energies (often termed Urbach energy [13]) greater than about 20 meV can result in significant radiative V_{oc} loss [14,15]. The latter conclusions are typically drawn from thermodynamic calculations that compare the ideal V_{oc} limit (i.e., no band tails) to that obtainable with sub-band-gap absorption and radiative recombination caused by band tails. Band-tail effects have also been incorporated into device models to study their implications on nonradiative recombination [16–18]. Herein, PL data are analyzed using a generalized model [19] to determine the key parameters associated with band tails for inclusion in device simulations. Although one recombination mechanism tends to dominate, an important distinction with band tails is that they can exacerbate all recombination channels by decreasing the effective activation energy.

Front-interface recombination is particularly important due to the polycrystalline *p*-*n* heterojunction in most TFPV devices. Poor conduction-band alignment and high defect density at the interface are known to increase recombination [20]. Measurements of current density versus voltage at various temperatures (JVT data) have identified that the front interface is often the primary recombination channel for various CdTe device architectures [21–25]. For the device studied here, JVT indicated a low V_{oc} activation energy that is likely associated with front-interface recombination. Care must be taken in the interpretation of JVT data to consider temperature and bias dependencies that can affect the observed activation energy [26], as discussed in Sec. IV.

This paper first presents an overview of recombination mechanisms and quantification of band-tail effects, along with the associated V_{oc} losses. In Sec. VI A, details are provided on the device under study. The results in Sec. III A combine analysis of several characterization techniques and device modeling to identify and estimate sources of V_{oc} loss. Suggestions on where to focus efforts on performance improvement are provided. The nuances associated with the V_{oc} activation energy, limitations of the method, and possible extensions of it are discussed in Sec. IV. Methodology is described after the conclusions in Sec. VI.

II. VOLTAGE LOSS MECHANISMS

A. Recombination

Open-circuit voltage V_{oc} is established in an illuminated photovoltaic device at a voltage such that the electron-hole pair generation current equals that due to recombination. Net current flow can be described by the conventional diode equation [27],

$$J = J_0\left[\exp\left(\frac{V - JR_s}{AkT/q}\right) - 1\right] + \frac{V - JR_s}{R_{sh}} - J_L(V), \quad (1)$$

where q is the elementary charge, A is the diode ideality factor, k is the Boltzmann constant, T is the temperature, R_s is the series resistance, R_{sh} is the shunt resistance, and $J_L(V)$ and J_0 are the photocurrent and saturation current densities, respectively. The photocurrent density $J_L(V)$ can be voltage-dependent, as discussed below. At $V = V_{oc}$, $J = 0$, and assuming $V_{oc} \gg kT/q$ and $R_{sh} \gg V_{oc}/J_L$, the balance of currents can be written as

$$J_L = J_0 \exp\left(\frac{qV_{oc}}{AkT}\right) = J_r + J_{nr} + J_f + J_b. \quad (2)$$

The recombination current densities are radiative (J_r), bulk nonradiative (J_{nr}), front interface (J_f), and back interface (J_b). All of the current densities in Eq. (2) are evaluated at $V = V_{oc}$. Figure 1 depicts them in a band energy diagram at V_{oc} and 1-sun light intensity. Well-known analytical estimates for the recombination current densities have been summarized in previous work in the context of TFPV [28–30]. Herein we calculate them numerically, so it suffices to mention that they are thermally activated and, typically, one of them tends to dominate such that the saturation current density, J_0, can be expressed in terms of an activation energy, E_a,

$$J_0 = J_{00} \exp\left(\frac{-E_a}{AkT}\right), \quad (3)$$

with J_{00}, E_a, and A dependent on the mechanism.

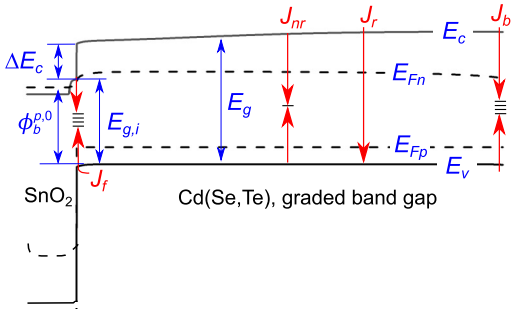

FIG. 1. Band edges of a Cd(Se, Te)/SnO_2 heterojunction at $V = V_{oc}$ and 1-sun light intensity showing front (J_f), bulk nonradiative (J_{nr}), radiative (J_r), and back (J_b) recombination current densities. Here E_c and E_v denote the conduction and valence bands; and E_{Fn} and E_{Fp} are the electron and hole quasi-Fermi levels. The bulk band gap, E_g, can differ from the front-interface band gap, $E_{g,i}$, due to a conduction-band offset, ΔE_c. For very high interface charge density, the electron quasi-Fermi level can be pinned at $\phi_b^{p,0}$.

The activation energy is determined by the dominant recombination pathway. For bulk mechanisms, J_r and J_{nr}, it is equal to the absorber band gap, $E_a = E_g$. At interfaces it may be equal to the interface band gap, $E_a = E_{g,i}$ if $E_{g,i} < E_g$. In that case, the conduction-band offset at a heterojunction can be determined by $\Delta E_c = E_{g,i} - E_g$. When J_f dominates and if charged interface defect densities are sufficiently high, the Fermi-level pinning energy above the valence band, $\phi_b^{p,0}$, can determine $E_a = \phi_b^{p,0}$ (see Fig. 1) [31].

Combining Eqs. (2) and (3) yields

$$qV_{\rm oc} = E_a - AkT\ln\left(\frac{J_{00}}{\eta_c(V_{\rm oc})J_{\rm sc}}\right). \tag{4}$$

A voltage-dependent collection efficiency, $\eta_c(V)$, accounts for photocurrent loss, $J_L(V_{\rm oc}) = \eta_c(V_{\rm oc})J_{\rm sc}$, where $J_{\rm sc}$ is the short-circuit current density [32]. The effects of η_c should be considered, especially in low-diffusion-length devices (see Sec. IV). Equation (4) indicates that $V_{\rm oc}$ is linear in T and, if plotted as a function of temperature, provides E_a as the ordinate intercept ($T \to 0$). However, E_a itself can be a function of temperature. Band-gap dependence on T can be approximated as linear near room temperature, $E_g(T) = E_{g0} - \beta T$ [33–35]. Typically, $\beta \sim 10^{-4}$ eV/K for direct-band-gap semiconductors and $E_g(T)$ becomes sublinear at lower temperature. As detailed below, band tails can also have a temperature-dependent E_a-lowering effect that we denote as $\Delta E_a(T)$. The activation energy at a given temperature is therefore

$$E_a(T) = E_{a0} - \beta T - \Delta E_a(T), \tag{5}$$

where E_{a0} is the $T = 0$ activation energy. The E_a in Eq. (4) should be replaced by Eq. (5). This implies that $V_{\rm oc}(T)$ is nonlinear if the band-gap and band-tail terms in Eq. (5) are nonlinear (see Sec. IV B).

Deviations from linearity of $V_{\rm oc}(T)$ are typically observed, especially at low temperature. For practical purposes, we focus on the region of normal operating temperatures and 1-sun light intensity (1 sun = 100 mW/cm^2). If $V_{\rm oc}(T)$ is linear over that range, then nonlinearities due to other temperature dependencies are reduced and, to a first approximation, the measured $E_a(T)$ is representative of the physical $V_{\rm oc}$ activation energy. If nonlinearity is observed at operating temperatures, then the ordinate intercept can significantly underestimate the actual activation energy. Nonlinearity, and variations with temperature and light intensity, are further discussed in Sec. IV.

The activation energy E_a can also be impacted by system disorder and bias dependencies. Next, we describe how band-tail impacts on E_a and $V_{\rm oc}$ can be incorporated in device models.

B. Band tails

Disorder in the semiconductor lattice can cause the otherwise abrupt densities of states at the conduction- and valence-band edges to extend into the band gap. These band tails result in increased absorption of photons with energy less than the unperturbed band gap, as well as increased recombination and, therefore, $V_{\rm oc}$ loss. In TFPV, common causes are: (i) band-gap fluctuations [36–38], due to variations in alloy composition, stoichiometry, and strain; and (ii) electrostatic fluctuations, due to charge inhomogeneity associated with doping, impurities, heavy compensation, and grain boundaries [39,40]. Tails manifest as sub-band-gap absorption and broadening of the luminescence peak, often accompanied by a red shift of the emission energy (PL peak) from the absorption energy.

The red shift from absorption to emission energy has been interpreted as a two-band-gap model with an absorption band gap, $E_{g,\rm abs}$, determined by the inflection of absorption or QE data, and a PL band gap, $E_{g,\rm PL}$, as the PL peak energy [15,38,41]. The result is an effective reduction of E_a in Eq. (4) by roughly $\Delta E_a = E_{g,\rm abs} - E_{g,\rm PL}$. Previous work has included that effect in device models by reducing the band gap by ΔE_a [16,17,42] or including an exponentially decaying distribution of trap states at the conduction- and valence-band edges [18]. For the device models herein, we employ the simple approach of reducing the band gap by ΔE_a, which governs recombination mechanisms. In doing so, the effect of the PL spectrum shape on the activation energy is not taken into account. This hypothesis is contrasted with more detailed approaches in Sec. IV.

In addition to E_a reduction, capturing band-tail effects in device models requires inputting the absorption coefficient, $\alpha(E)$, with the appropriate low-energy tail. Herein, we determined it from PL data. The functional form of $\alpha(E)$ depends on the underlying microscopic cause of the band tails. However, a generalized model [19] expresses it as

$$\alpha(E) = \alpha_0\sqrt{\gamma}\,G\left(\frac{E - E_g}{\gamma}\right)(f_v - f_c), \tag{6}$$

where E is photon energy, E_g is the unperturbed band gap, and γ is the characteristic decay energy. For a direct-band-gap semiconductor, $\alpha_0 \sim 10^5$ cm^{-1} eV$^{-1/2}$ and $G(x)$ is the convolution of tail states with the typical square-root density of states (DOS) for the conduction and valence bands,

$$G(x) = \frac{1}{2\Gamma(1 + 1/\theta)}\int_{-\infty}^{\infty}\exp\left(-|x|^{\theta}\right)\sqrt{x - x'}\,dx'. \tag{7}$$

The normalization term includes the gamma function $\Gamma(1 + 1/\theta)$. Only the real part of Eq. (7) is required. The θ parameter depends on the band-tail model: $\theta = 1$ is Urbach

[13]; $\theta = 5/4$ is screened Thomas-Fermi [40]; $\theta = 3/2$ is Franz-Keldysh; and $\theta = 2$ is semiclassical Thomas-Fermi [43]. When $\theta = 2$, the form of $\alpha(E)$ is similar to the "Gaussian distribution of band gaps" model [36], discussed in Sec. IV.

In Eq. (6), the band filling factor is [19,44]

$$f_v - f_c = \tanh\left(\frac{E - \Delta\mu}{4kT}\right), \tag{8}$$

where f_v and f_c are the valence- and conduction-band occupancies for a given quasi-Fermi-level splitting, $\Delta\mu$. Band filling results in bias-dependent absorption and QE [17], and improved fitting of PL spectra when band tails are present [15]. Equation (8) is an approximation based on the Fermi-Dirac distribution, assuming bands with parabolic dispersion and equal electron and hole effective masses.

The absorptance is approximated as

$$a(E) = 1 - e^{-\alpha(E)d}, \tag{9}$$

where d is the lesser of the device thickness or the sum of the absorption length $(1/\alpha)$ and the diffusion length of the minority carriers in the absorber. The absorptance can be expressed to include optical corrections for multilayer thin-film structures [45] and interference effects [46], especially when the absorber layer is relatively thin compared to the absorption depth. Finally, from the generalized Planck law [47], the PL flux can be expressed as

$$I_{\mathrm{PL}}(E) = \frac{2\pi a(E)}{h^3c^2}\frac{E^2}{\exp\{(E - \Delta\mu)/kT\} - 1}, \tag{10}$$

where h is the Planck constant and c is the speed of light. Absolute PL data at 1-sun equivalent light intensity and room temperature were fit using Eqs. (6)–(10) with parameters θ, γ, $\Delta\mu$, T, and E_g. Using $E_g = E_{g,\mathrm{abs}}$ and reasonable starting values for $\Delta\mu$ and T (which mostly control peak height), the most sensitive parameters are θ and γ (which mostly control peak energy and skewness, respectively). Parameters θ and γ provide clues for the band-tail DOS shape and extent. Note that the fitting parameter values also yield the peak energy, $E_{g,\mathrm{PL}}$. From the above analysis, $\alpha(E)$ and a uniform band-gap reduction of $\Delta E_a = E_{g,\mathrm{abs}} - E_{g,\mathrm{PL}}$ are used in the device models. Note that γ defines the energetic extent of the absorption coefficient tail, but it is not a direct simulation input. This approach is only considered reasonable if the PL data are well fit by this band-tail model and not dominated by other features, such as shallow localized states [45].

Alternative approaches to this generalized PL model have been presented. Spaans *et al.* [46] employed this same model as Ref. [19] and added to it a Gaussian fluctuation of band-gap energies [36,37]. That unified model increases the number of fitting parameters and it assumes *a priori* a Gaussian distribution of band gaps, which may not be appropriate in general or for our Cd(Se, Te) case study. Rey *et al.* [48] also considered a hybrid approach that combined electrostatic potential and band-gap fluctuations. The band-gap distribution was again restricted to Gaussian and was used to study band tails in kesterite TFPV devices. It is our perspective that the shape of the band tails is unknown and should be a flexible parameter in PL data analysis.

III. RESULTS

A. Device-level analysis

To demonstrate the voltage loss evaluation method, one exemplary NREL (National Renewable Energy Laboratory) device was subjected to several characterization techniques. The device stack consisted of SnO_2:F/SnO_2/Cd(Se, Te) in superstrate configuration. The 3-μm thick absorber was As-doped and had a graded Se profile, resulting in a graded band gap. Fabrication details are provided in Sec. VI A. This research-based device had an efficiency of $\eta = 15.9\%$ and $V_{\mathrm{oc}} = 744$ mV. The V_{oc} deficit is rather large at $V_{\mathrm{oc,rad}}^{\mathrm{ideal}} - V_{\mathrm{oc}} = 402$ mV, where $V_{\mathrm{oc,rad}}^{\mathrm{ideal}} = 1.146$ V is the SQ limit [calculated below, cf. Eq. (11)] for $E_g = 1.415$ eV. The latter value was used as the effective band gap when band tails are not present and was derived from the inflection point of QE data [49], as described in Sec. II B. Determining where and to what extent voltage losses occur are key challenges. A simulated band-edge diagram for this device at V_{oc} is shown in Fig. 1.

It is useful to first check the JVTi data for signs of low-activation-energy issues. A plot of V_{oc} as a function of temperature and over a range of light intensities (1 sun = 100 mW/cm^2 of AM1.5G spectrum illumination), extracted from the JVTi data, is shown in Fig. 2. From the high-temperature linear region ($T > 290$ K), the intercept is $E_{a0} = 1.470 \pm 0.014$ eV at 0.02 suns, decreasing to $E_{a0} = 1.137 \pm 0.033$ eV at 1.78 suns. For practical purposes, our focus is on V_{oc} loss diagnosis near operating conditions, where the higher-temperature linear regime interpolated to 1 sun yields $E_{a0} = 1.246 \pm 0.036$ eV, well below the room-temperature graded-band-gap range of 1.4–1.5 eV. The saturation of V_{oc} as temperature decreases is often observed for polycrystalline devices [26,30]. The low-light and low-temperature behaviors are interesting and discussed further in Sec. IV.

Accounting for E_g temperature dependence from Eq. (5), and using $\beta = 10^{-4}$ eV/K, yields $E_a = 1.216 \pm 0.036$ eV at $T = 300$ K. That suggests a clifflike conduction-band offset, $\Delta E_c = E_a - E_g \approx -0.2 \pm 0.036$ eV, at the front interface (assuming $E_g = 1.415$ eV, and neglecting band-tail-induced lowering for the moment). The uncertainty is discussed further in Sec. IV D. To study the relationship between ΔE_c and E_a, we simulated JVTi using a numerical device model tailored for this specific device. A broad parameter space was studied with

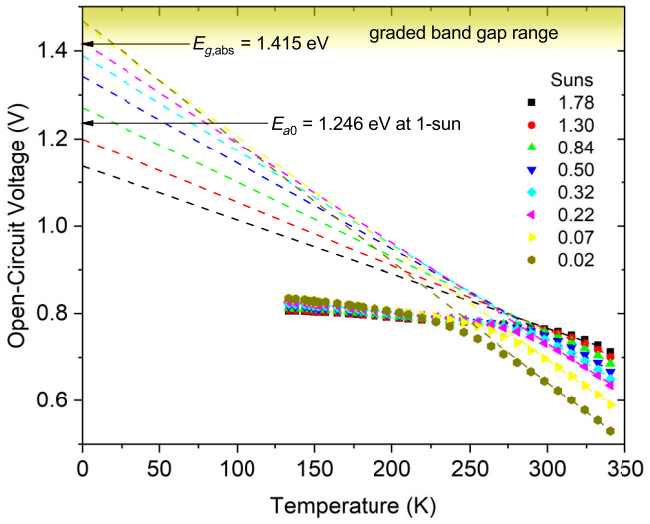

FIG. 2. Open-circuit voltage as a function of temperature at the light intensities shown in suns (1 sun = 100 mW/cm^2). Linear fits of the high-temperature region provide the activation energy, E_{a0}. The absorption band gap, $E_{g,\mathrm{abs}}$, from the QE inflection point is also shown. The graded band-gap range at room temperature is shown as the yellow shaded region.

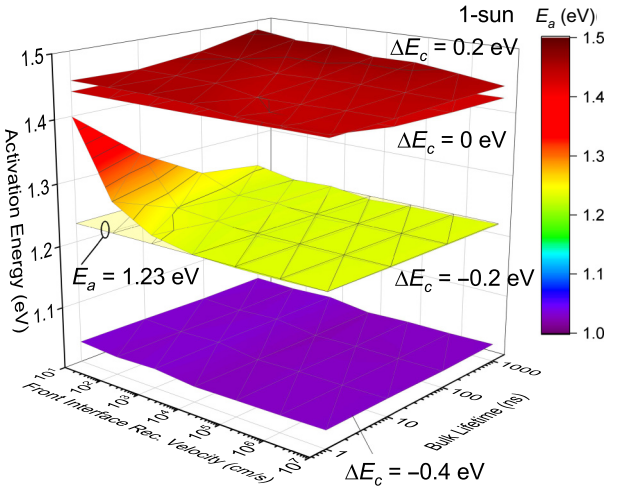

FIG. 3. Activation energies from simulated JVTi at 1-sun light intensity at various front-interface conduction-band offsets ($\Delta E_c < 0$ eV is a cliff alignment). Front-interface recombination velocity, S_f, and bulk nonradiative lifetime, τ, are on the x and y axes, respectively. The flat plane indicates an activation energy of 1.23 eV, within the range of the measured 1.216 ± 0.036 eV, after correcting for the band-gap temperature dependence.

$\Delta E_c = -0.4$ to 0.2 eV, front-surface recombination velocity $S_f = 10$–10^7 cm/s, back-surface recombination velocity $S_b = 10$–10^7 cm/s, and equal electron and hole lifetimes of $\tau = 1$–1000 ns. To test the front-interface and bulk effects, the back-contact recombination velocity was initially set to a constant $S_b = 10^5$ cm/s. Simulations spanned $T = 250$–350 K and intensity 0.001–1 sun. The simulation methodology is provided in Sec. VI C, and parameter values are provided in the Supplemental Material [50].

A subset of the simulation results, shown in Fig. 3, indicates that, at 1 sun, $E_a \approx 1.23$ eV can be realized only for $\Delta E_c = -0.2$ eV, but for any $S_f \geq 10^3$ cm/s and $\tau \geq 1$ ns. Flat-band and positive (spike) alignment result in $E_a \approx E_g$, whereas, for the large cliff at $\Delta E_c = -0.4$ eV, E_a is due to the front-interface offset for all S_f and τ. Note that, for $\Delta E_c = -0.2$ eV, there is a transition from front-interface to bulk recombination (E_a increasing from 1.23 toward 1.40 eV) when S_f and τ are both relatively low.

Using $\Delta E_c = -0.2$ eV, simulations were compared to $V_{\mathrm{oc}}(T)$ data to narrow down the possible range of S_f and τ. Figure 4 shows $V_{\mathrm{oc}}(T)$ over the full range of S_f and τ at 1-sun intensity. The simulations (shaded regions) and data (points) are similar for $S_f \sim 10^3$–10^4 cm/s. Bulk lifetime remains unknown and is at least within $\tau = 1$–1000 ns, which implies that front-interface recombination dominates V_{oc} loss under these conditions, even for the lowest bulk lifetime of $\tau = 1$ ns. It is evident in Fig. 4 that V_{oc} becomes less sensitive to τ as S_f increases. Note that the simulations do not include certain temperature-dependent effects that play an important role in $V_{\mathrm{oc}}(T)$, especially at $T < 300$ K (see Sec. IV).

Bulk lifetime was further assessed by studying QE and TRPL data. Using $\Delta E_c = -0.2$ eV and $S_f = 10^3$ cm/s, comparison of the simulated and measured QE in Fig. 5 suggests that a low value of $\tau \approx 1$ ns could account for

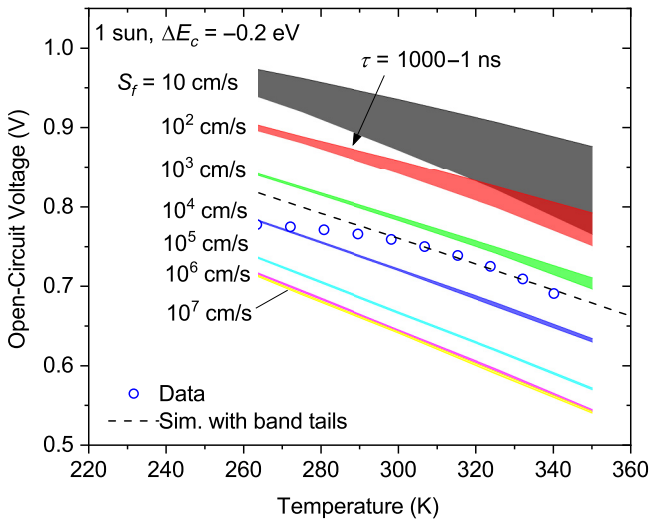

FIG. 4. Open-circuit voltage as a function of temperature at 1-sun light intensity. Each shaded region (simulation) is for front-interface offset $\Delta E_c = -0.2$ eV and indicated front-interface recombination velocity, S_f, within a range of bulk nonradiative lifetime $\tau = 1$–1000 ns (shaded regions). Data (points) fall between $S_f = 10^3$ and 10^4 cm/s. Band tails are included in the simulation (dashed line) with the parameter values discussed in the text.

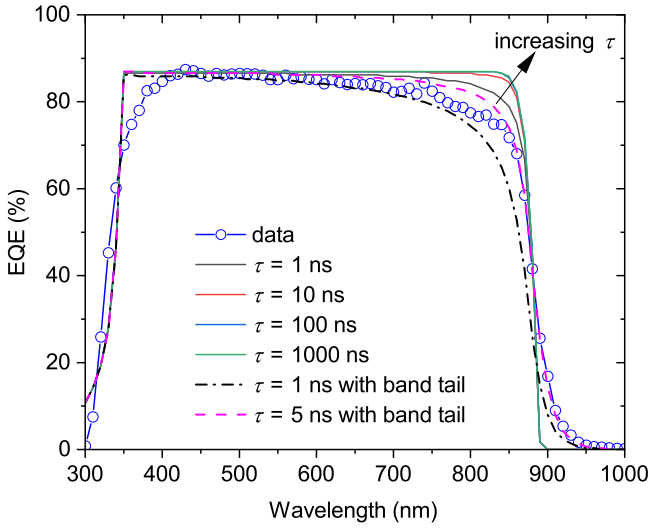

FIG. 5. Measured (points) and simulated (lines) external quantum efficiency (EQE). Simulations without band tails include front-interface recombination velocity $S_f = 1000$ cm/s and band offset $\Delta E_c = -0.2$ eV with nonradiative bulk lifetimes $\tau =$ 1–1000 ns. Simulation with band-tail effects used $\tau = 1$ (dashed-dotted) and 5 ns (dashed).

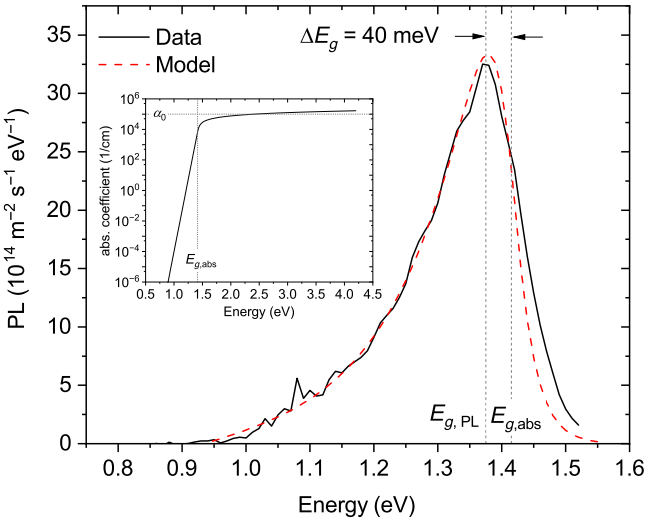

FIG. 6. Absolute PL at 1-sun light intensity (black) compared to the generalized model [Eqs. (6)–(10), dashed line]. The $E_{g,\mathrm{abs}}$ value was obtained from the QE inflection point and compared to the PL peak, $E_{g,\mathrm{PL}}$, to obtain the tail-induced band-gap shift, ΔE_g.

the lower carrier collection at longer wavelengths. Additional QE simulations indicated that increasing S_f with fixed $\tau = 1$ ns resulted in declining carrier collection at shorter wavelengths, contrary to observations, thereby corroborating $S_f \sim 10^3$–10^4 cm/s (see Supplemental Material [50]). Near the band-gap energy, QE simulations have a steeper decline compared to the data. Band-tail effects can account for that QE broadening, as discussed below.

TRPL data and simulations indicate decay times of $\tau \lesssim 1$ ns when using the parameter values $\Delta E_c = -0.2$ eV, $S_f = 10^3$ cm/s, and $\tau \approx 1$ ns (see Supplemental Material [50]). Simulations enable visualization of charge transport and/or recombination processes. They indicate that the junction electric field is mostly screened by injected charge within 0.1 ns after excitation. During the first 2 ns of decay, most of the recombination is at the front surface for the lower-wavelength excitation (405 nm) and close to evenly split between bulk and front interface for the higher wavelength (670 nm). In both cases, during that time period, charge diffusion proceeds as electrons and holes flow toward the back surface. However, the 405-nm decay was slower than the 670-nm excitation decay due to the higher fluence at 670 nm. That higher fluence by 7.5 times resulted in a high injection state (hole density greater than acceptor doping) and therefore shorter lifetime. TRPL simulations agree with the data, but it is difficult to distinguish interface from bulk recombination with single TRPL measurements.

Simulation results thus far have provided initial estimates of $\Delta E_c = -0.2$ eV, $S_f = 10^3$–10^4 cm/s, and $\tau = 1$ ns, without accounting for band-tail effects. Figure 6 shows absolute PL data at 1-sun equivalent light intensity compared to the model described in Sec. II B. Least-squares fitting yielded band-tail parameters $\theta = 1$, $\gamma = 22$ meV, and $\Delta\mu = 0.710$ eV, using fixed values of $E_g = 1.415$ eV and $T = 300$ K. The resulting absorption coefficient from Eq. (6) is shown in the inset to Fig. 6. The PL peak energy is $E_{g,\mathrm{PL}} = 1.375$ eV. A Gaussian fit of $d(QE)/dE$ yields the absorption band gap $E_{g,\mathrm{abs}} = 1.415$ eV (see Supplemental Material [50]). The tail-induced energy shift is $\Delta E_a = 40$ meV and, as described in Sec. II B, the graded band gap in the device models was reduced by 40 meV. Estimates of $\Delta E_a = 40$–70 meV using different methods are provided in Sec. IV A. With the reduced band gap, it was required also to decrease the conduction-band offset ΔE_c from -0.200 to -0.160 eV to maintain the observed $E_a = 1.216$ eV.

The PL model fit in Fig. 6 underestimates the data at higher photon energy. Typical fitting of the PL emission high-energy slope is shown in the Supplemental Material [50], where the best-fit line yields $T = 370$ K, which is too high due to low photoluminescence quantum yield (PLQY) and high background noise for this sample. That fit also yields $\Delta\mu = 0.56$ V, which is too low given the device $V_{\mathrm{oc}} \approx 0.74$ V. Similar fitting uncertainties were discussed in Ref. [51]. We know that the sample temperature is much lower than 370 K – thin-film samples with similar thickness and grown on similar substrates but with higher PLQY typically yield $T = 300$ K. Constraining the temperature to 300 K yields the poor fit shown in green in Fig. S6 in the Supplemental Material [50], for which $\Delta\mu = 0.74$ V – in agreement with device voltage. As stated earlier, the poor high-energy fit is due to low PLQY and resulting

higher background. Instead, we use full spectral analysis with a reasonable adjusted $R^2 = 0.989$. At $E < E_{g,\mathrm{abs}}$, the critical features of red shift, ΔE_a, and band-tail characteristic energy, γ, are effectively captured by the generalized PL model.

To summarize, the dashed line in Fig. 4 is the simulated $V_{\mathrm{oc}}(T)$ for the case with $\Delta E_c = -0.160$ eV, $S_f = 2000$ cm/s, $\tau = 5$ ns, and $\Delta E_a = 40$ meV, along with $\alpha(E)$ extracted from PL data. With the same parameter values, QE broadens at longer wavelengths in accordance with the data (see Fig. 5). However, QE comparison indicated that $\tau = 1$ ns is too low when band tails are added because of lower recombination activation energy. When band tails are present, the QE data are better fit with $\tau = 5$ ns, as shown by the magenta dashed line in Fig. 5.

Incidentally, fitting the absolute PL spectrum provides the absorptance from Eq. (9) and enables calculation of the radiative voltage limit [6]

$$V_{\mathrm{oc,rad}} = \frac{kT}{q} \ln\left(\frac{\int a(E)\phi_{\mathrm{exc}}(E)\,dE}{\int a(E)\phi_{\mathrm{bb}}(E)\,dE} + 1\right), \tag{11}$$

where ϕ_{exc} and ϕ_{bb} are the excitation and black-body spectra. Ideally, the absorptance is a step function and Eq. (11) provides the SQ limit of $V_{\mathrm{oc,rad}}^{\mathrm{ideal}} = 1.146$ V at $T = 298$ K. Using the absorptance from the PL spectrum fit with the $\gamma = 22$ meV band tails gives $V_{\mathrm{oc,rad}} = 1.089$ V, a loss of 57 mV. The radiative loss can also be estimated from the QE data, as described in Ref. [49]. The implied voltage can then be determined, $iV_{\mathrm{oc}} = V_{\mathrm{oc,rad}} + kT/q \ln(\mathrm{PLQY}) = 707$ mV, very close to the quasi-Fermi-level splitting, $\Delta\mu = 710$ mV from the fitting. The band-tail loss of 57 mV is within the range of 40–70 mV calculated in Sec. IV.

B. Photoemission spectroscopy: Band alignment

A key result in the above analysis is the presence of a clifflike conduction-band offset. Front-interface band alignment was independently measured using a combination of XPS, UPS, and LEIPS on thermomechanically cleaved devices [52] (see Sec. VI for methodology). Relevant graphical data are provided in the Supplemental Material [50]. The results are in agreement with the ΔE_c range estimated above.

Figure S7 in the Supplemental Material [50] shows XPS survey spectra of each side of the liquid-nitrogen-cleaved device. As we have shown previously, cryogenic cleaving of these devices occurs within an atomically thin layer of the layered compound $CdCl_2$ that resides at the SnO_2/Cd(Se, Te) interface [53]. $CdCl_2$ is introduced during fabrication (see Sec. IV A). Residual pockets of Cd(Se, Te) absorber that remained on the SnO_2 side, identified by tellurium signals in Fig. S7, allowed location of the absorber band positions at the SnO_2 interface by the methods described below.

Figure S8 in the Supplemental Material [50] comprises photoemission data taken on the Cd(Se, Te) side of the cleaved device that was used to determine core-level to valence-band energies for the Cd(Se, Te) alloy as it exists near the SnO_2 interface. To account for possible photovoltages in UPS data, the core-level XPS spectrum of the Te $3d_{5/2}$ region in Fig. S8(a) was obtained with the UPS light source on. The main component was found at 572.78 eV. In Fig. S8(b), UPS data plotted logarithmically to emphasize the low density of states [54] show 0.67 eV from the valence-band maximum (VBM) to the Fermi energy (E_F) near the surface of the bare absorber, yielding a Te $3d_{5/2}$ to VBM energy difference of 572.11 eV for the particular composition of Cd(Se, Te) used here.

XPS spectra from the SnO_2 side and of the Te $3d_{5/2}$ region show that tellurium detected here represents the Cd(Se, Te) absorber as judged by the line shape and peak position of Fig. S9 in the Supplemental Material [50]. Some oxidized Te^0 was revealed by curve fitting, with the Te^0 chemical component located at 0.6 eV higher in energy than the lattice Te^{2-}. Using the previously determined Te $3d_{5/2}$ to VBM core-level difference and the location of the Te^{2-} component at 573.06 eV, the Cd(Se, Te) VBM is found to be 0.96 eV below the Fermi energy at the SnO_2 interface. From the XPS-measured Se : (Se + Te) ratio and the published bowing curve for Cd(Se, Te) [55], the near-interface band gap is 1.43 eV and the conduction-band minimum (CBM) is located 0.48 eV above E_F.

LEIPS from the SnO_2 side of the cleaved device are shown in Fig. S10 in the Supplemental Material [50]. These data represent primarily the SnO_2 conduction band, with the CBM being located at 0.27 eV above E_F. Together with the data from Fig. S9, the Cd(Se, Te)/SnO_2 alignment is shown in Fig. 7, indicating a 0.21-eV clifflike CBM alignment between the SnO_2 and Cd(Se, Te) absorber. Error analysis provided in the Supplemental Material [50] indicates $\Delta E_c = -0.21 \pm 0.12$ eV [56]. Assuming a normal distribution, that implies a most probable value of -0.21 eV, with deviations becoming increasingly unlikely as one moves away from the center of the distribution [57]. The resulting interface band gap of 1.23 eV is within

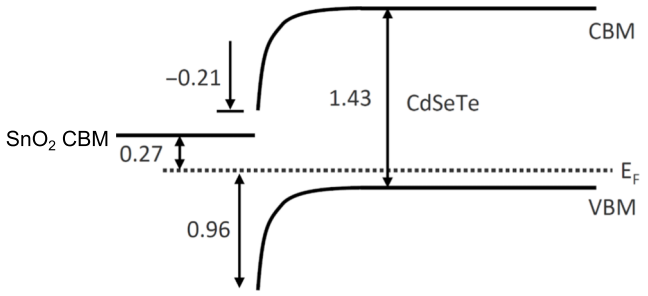

FIG. 7. Schematic of SnO_2/Cd(Se, Te) band alignment from UPS, XPS, and LEIPS.

TABLE I. Simulated V_{oc} losses compared to an ideal case, models 1 and 1T. Models with "T" include band-tails effect (quantified by γ). Front-interface recombination (due to ΔE_c and S_f) dominates for models 2 and 2T. Bulk nonradiative recombination (due to τ) dominates for models 3 and 3T. Combined effects are models 4 and 4T. Back-interface recombination velocity is $S_b = 10^5$ cm/s and series resistance $R_s = 0$ in all cases.

	Ideal		Front		Bulk		Combined	
Model	1	1T	2	2T	3	3T	4	4T
Inputs								
ΔE_c (eV)	0	0	−0.16	−0.16	0	0	−0.16	−0.16
S_f (cm/s)	10^2	10^2	4×10^3	4×10^3	10^2	10^2	4×10^3	4×10^3
τ (ns)	10^3	10^3	10^3	10^3	5	5	5	5
γ (meV)	0	22	0	22	0	22	0	22
Outputs								
η (%)	25.9	25.1	19.4	18.6	21.0	19.3	18.9	17.2
J_{sc} (mA/cm^2)	29.5	29.9	29.4	29.8	29.4	28.8	29.3	28.7
V_{oc} (V)	1.00	0.96	0.79	0.75	0.88	0.84	0.78	0.74
ΔV_{oc} (V)	0	0.04	0.21	0.25	0.12	0.16	0.21	0.26

the activation energy range determined from $V_{oc}(T)$ (cf. Figure 2).

C. V_{oc} loss breakdown

Using the parameter values estimated above, we consider the voltage losses associated with the front-interface, bulk, and band-tail mechanisms. Key parameter values and results are listed in Table I. An "idealized" model with overall very low recombination and $\Delta E_c = 0$ acts as a reference to which the other cases are compared to quantify the voltage loss, ΔV_{oc}, as given in the last row. All models had $S_b = 10^5$ cm/s at the back contact and series resistance $R_s = 0\ \Omega\ \text{cm}^2$. The ideal model had $V_{oc} = 1$ V without band tails (model 1) and 0.96 V with band tails (model 1T, "T" indicates that band tails are included). Tails are characterized by $\gamma = 22$ meV and $\Delta E_a = 40$ meV. With tails, efficiency declined by about 3% relative, mostly due to V_{oc} with some J_{sc} increase. Values of V_{oc} for models with dominant front-interface losses (due to higher S_f and with $\Delta E_c = -0.160$ eV, models 2 and 2T) and dominant bulk losses (due to lower τ, models 3 and 3T), with and without band tails, are provided. Front losses alone reduce V_{oc} from 1 V to 0.79 V and down to 0.75 V with the addition of band tails. That comprised nearly all of the loss for the measured $V_{oc} = 0.744$ V. The efficiency remains relatively high for model 2 due to high J_{sc} given the long bulk lifetime. Bulk recombination on its own results in $V_{oc} = 0.88$ and 0.84 V without and with band tails, respectively. Combining front, bulk, and band-tail losses yields $V_{oc} = 0.74$ V, listed as the combined model (models 4 and 4T). The efficiency of model 4T would decrease from $\eta = 17.2\%$ to 16.1% if series resistance and a back-contact barrier were added to reduce the fill factor (cf. Fig. 9).

The results in Table I suggest that the front interface is the greatest source of V_{oc} loss. Minimizing front-interface recombination would limit V_{oc} to 0.84 V due to bulk recombination. To investigate this further, Fig. 8 shows the individual recombination current densities from Eq. (2) as functions of voltage at 1-sun light intensity and $T = 300$ K. At V_{oc}, shown as the vertical line, the recombination currents sum to the photogeneration current $J_L = 29.5\ \text{mA/cm}^2$. For the device under study, based on model 4T in Table I, Fig. 8(a) indicates that front-surface recombination, $J_f = 26\ \text{mA/cm}^2$, is responsible for most of the voltage loss, with bulk nonradiative $J_{nr} = 3.25\ \text{mA/cm}^2$, and back interface $J_b = 0.25\ \text{mA/cm}^2$ making up the rest. However, for $V < 0.63$ V, bulk nonradiative recombination, J_{nr}, becomes dominant. That may be one possible

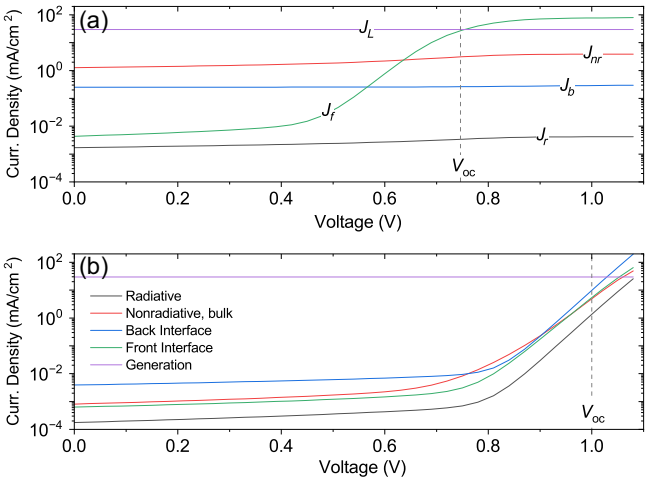

FIG. 8. Simulated recombination and photogeneration current densities [cf. Eq. (2)] as functions of applied bias for (a) the case study device given by model 4T in Table I, and (b) the ideal model 1. For each device, V_{oc} is shown as the dashed line. Simulations were at $T = 300$ K and 1-sun light intensity.

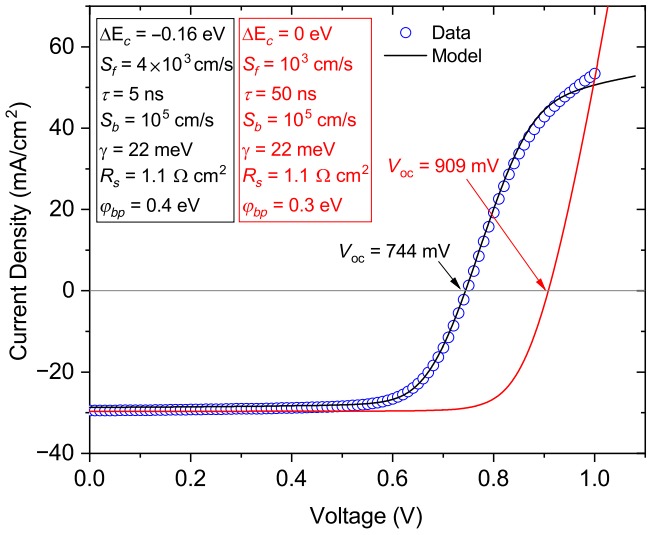

FIG. 9. JV data (points) for the device under study compared to the model with parameters determined here (black text) and to a device with practical improvements in conduction-band alignment and bulk lifetime (red text). Key parameter values are shown inset, as defined in the text.

explanation for the observed E_a increase from $E_{g,i}$ to bulk E_g as light intensity, and therefore V_{oc}, decreased (see Fig. 2); the same notion was proposed in Ref. [30].

Figure 8(b) shows that, for the ideal case of model 1 in Table I, the recombination current is greatest for the back interface, $J_b = 11.9$ mA/cm^2, with the rest nearly equal, $J_f = 6.3$ mA/cm^2, $J_{nr} = 5.8$ mA/cm^2, and $J_r = 5.4$ mA/cm^2. If all nonradiative losses were further reduced, radiative recombination would become dominant (i.e., radiative limit).

Given the above analysis, it is interesting to consider what modifications can produce a Cd(Se, Te) device with $V_{oc} \gtrsim 0.90$ V, comparable to the current record. Figure 9 shows the simulated current density versus voltage (JV data) using the parameter values determined above (model 4T in Table I) overlain with the data. A series resistance $R_s = 1.1$ Ω cm^2 and a back-contact hole barrier $\varphi_{bp} = 0.4$ eV were added to match the slope near V_{oc} and the current saturation ("roll-over") at higher voltage, respectively. Increasing V_{oc} from 0.744 to 0.909 V was achieved by setting $\Delta E_c = 0$ eV and $S_f = 10^3$ cm/s (to minimize front-interface issues) and increasing τ from 5 to 50 ns. Roll-over was eliminated by reducing φ_{bp} to 0.3 eV. Those modifications lead to an efficiency increase from $\eta = 16.1\%$ to 21.8%. Analysis of recombination currents, as in Fig. 8, showed that most of the V_{oc} loss was in the bulk absorber ($J_{nr} = 19$ mA/cm^2), with lower contributions from the front interface ($J_f = 9$ mA/cm^2) and back contact ($J_b = 1.5$ mA/cm^2). Simulations also indicated that varying φ_{bp} from 0.1 to 0.4 eV did not affect V_{oc}, but reduced fill factor and enhanced roll-over.

IV. DISCUSSION

Disorder and nonidealities associated with thin-film polycrystalline systems create challenges for V_{oc} loss assessment that may be subdued for crystalline devices. The effects discussed in this section, such as band tails, and the sensitivity of the V_{oc} activation energy to temperature and light, can result in misleading device-level characterization and standard diode analysis. Furthermore, techniques that inspect device properties at various levels of completion are questionable, since device properties evolve during the course of fabrication. Finally, for a multimode characterization approach, devices that exhibit any metastability should undergo the same preconditioning procedure before every measurement.

A. Interpretation of V_{oc} loss due to band tails

In device models with band tails, the graded band gap was uniformly reduced by the Stokes shift, $\Delta E_a = E_{g,\mathrm{abs}} - E_{g,\mathrm{PL}}$ [16,17] (also discussed in Ref. [58]), and the absorption coefficient was obtained by fitting the full PL spectrum. The Stokes shift is a voltage penalty due to carrier thermalization to a lower energy due to band tails [15]. It has been shown that using ΔE_a in this way can overestimate radiative losses by $\sim$ 10–20 mV in many cases [59]. That range is within our activation energy uncertainty of ± 0.036 eV. Here we consider other methods by which to calculate ΔE_a and its dependence on the tail decay energy, γ.

Closer examination of the relationship between the observed PL and ΔE_a can be sought by noting that the radiative recombination current density can be expressed as

$$J_r = q \int I_{\mathrm{PL}}\, dE = J_{00,r} \exp\left(-\frac{E_a - \Delta\mu}{AkT}\right), \qquad (12)$$

where $J_{00,r}$ is the pre-exponential for radiative recombination, in connection with Eqs. (2) and (3). In the ideal case, $E_a = E_g$ (i.e., the unperturbed band gap, $\Delta E_a = 0$). Numerical integration of Eq. (12), with I_{PL} given by Eq. (10), over the temperature range $T = 200$–450 K is shown in the Arrhenius plot of Fig. 10. To obtain the dependence of E_a on γ and temperature, as part of the numerical analysis, we assume that $\Delta\mu$ and γ are temperature-independent and $A = 1$. Solid points in Fig. 10 represent band-tail parameter values that were used in Fig. 6. For $\gamma = 22$ meV and $T \geq 300$ K, the slope gives $E_a - \Delta\mu = 0.649$ eV, or $E_a = 1.359$ eV, for $\Delta\mu = 0.710$ eV (neglecting the nonlinear temperature dependence of V_{oc} for the moment). In this case, the band-gap reduction due to tails is $\Delta E_a = 1.415 - 1.359 = 56$ meV, which is slightly larger than the 40 meV shown in Fig. 6. However, it is quite close to the 57 meV calculated as the difference for $V_{oc,\mathrm{rad}}$ with and without band tails [cf. Eq. (11)]. Note

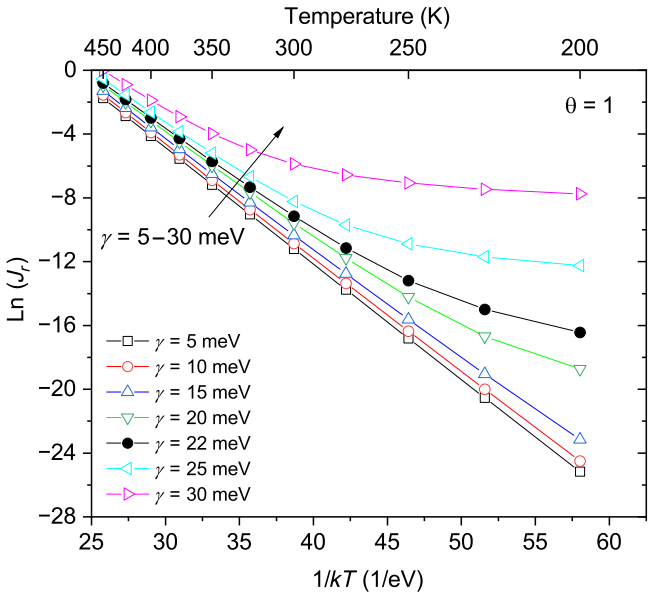

FIG. 10. Arrhenius plot of J_r from Eq. (12) for $\gamma = 5$–30 meV, $\theta = 1$, $\Delta\mu = 0.710$ eV, and $E_g = 1.415$ eV. The value $\gamma = 22$ meV (solid points) provides the same band-tail settings as the model in Fig. 6.

that this E_a is related to the bulk band gap, while E_a in Sec. III A is the interface band gap. It is also noteworthy that the integral of Eq. (12) yields $J_r \sim 10^{-3}$ mA/cm^2, on the same order as J_r from the device model shown in Fig. 8(a).

Activation energies for different γ were also obtained from Fig. 10. For small tails up to $\gamma = 15$ meV, $E_a \gtrsim 1.41$ eV and is relatively constant with T. For $\gamma > 15$ meV, E_a becomes increasingly temperature-dependent and it decreases with temperature until saturating when the slope goes to zero, $E_a = \Delta\mu$. It has been shown [15] that the activation energy decreases rapidly for $\gamma \gtrsim kT$, then saturates near $\Delta\mu$. These results are for $\theta = 1$ and the effects are reduced as θ increases, but the results are qualitatively the same. Additional temperature dependencies can affect E_a, as discussed in Sec. IV B.

An alternative approach to estimating band-tail-induced V_{oc} loss considered a Gaussian distribution of band gaps. The derived absorptance was [31,37,60,61]

$$a = \frac{1}{2}\,\mathrm{erfc}\left(\frac{E_g - E}{\sqrt{2}\,\sigma}\right). \tag{13}$$

The integration of Eq. (12) using Eqs. (10) and (13) provided the activation energy reduction

$$\Delta E_a = \frac{\sigma^2}{2AkT}. \tag{14}$$

Equation (14) holds for a Gaussian distribution of fluctuations with standard deviation σ [36]. For band-gap fluctuations, σ is the standard deviation of the band-gap distribution in the absorber. In the case of potential fluctuations, σ can be related to charged dopant and compensating impurity distributions [43,62] (σ was denoted σ_{elec} in Ref. [63]).

As in previous work [38,49], here we obtained σ by fitting the first derivative of the QE absorption edge, $d(QE)/dE$, to a Gaussian function, providing $\sigma = 62$ meV, as shown in the Supplemental Material [50]. A value $\sigma = 15$–65 meV was reported for Cu(In,Ga)Se$_2$ (CIGS) [37,38], and a numerically estimated value $\sigma = 20$–70 for Cd(Se, Te) [63]. For $\sigma = 62$ meV, Eq. (14) yields $\Delta E_a = 37$ to 74 meV for $A = 2$ to 1.

Of the four approaches discussed, $\Delta E_a \approx 40$–70 meV is a reasonable range to use in the device models at normal operating temperatures, suggesting 55 ± 15 meV. However, as shown in the Supplemental Material [50], the Gaussian distribution model from Eqs. (10) and (13) with $\sigma = 62$ meV cannot fit the PL data. It produces a more symmetric PL spectrum, similar to the generalized model with $\theta = 2$ and $\gamma = 62$ meV in Eq. (7), also shown in the Supplemental Material [50]. Regardless of the microscopic cause, the hypothesis that increasing γ reduces the effective band gap and, therefore, increases all thermally activated recombination mechanisms, appears to be warranted [37]. Hence, interface band gaps are also reduced for a given conduction-band offset, thereby increasing interface recombination.

B. Temperature dependence of activation energy

It is evident from Fig. 2 that E_a depends on temperature and $V_{oc}(T)$ can be nonlinear, especially at low temperature, contrary to Eq. (4). Nuances with interpreting E_a must be considered to question the validity of assigning the room-temperature E_a to the front-interface band gap (related to conduction-band offset), as done above and in several previous reports [21–25,28].

Band-gap and band-tail temperature dependencies were implicit in Eq. (5). Figure 10 and Eq. (14) both indicate decreasing E_a with decreasing temperature due to band tails. That dependence on the interpretation of $V_{oc}(T)$ was also considered in Ref. [26]. For the band-tail parameters determined above from PL data ($\theta = 1$, $\gamma = 22$ meV), Fig. 10 indicates that E_a is relatively temperature-independent for $T \geq 300$ K.

Further analysis includes possible temperature dependencies of A, η_c, and J_{00} from Eq. (4). Any significant T dependence of those terms would result in a deviation from linearity in $V_{oc}(T)$, which appears to be minimal in our range of concern, 300–350 K. The curvature observed at $T \lesssim 300$ K can be evaluated by inserting Eq. (5) into Eq. (4) and expanding to first order near reference temperature T_0. Taking the limit $T \to 0$ yields the

temperature-dependent ordinate intercept:

$$\lim_{T\to 0} qV_{\rm oc} = E_{a0} - \Delta E_a(T_0) + T_0 \frac{d(\Delta E_a)}{dT}\bigg|_{T_0} + kT_0^2 \ln\left(\frac{J_{00}}{\eta_c J_{\rm sc}}\right)\frac{dA}{dT}\bigg|_{T_0} + AkT_0^2 \frac{d}{dT}\left[\ln\left(\frac{J_{00}}{\eta_c J_{\rm sc}}\right)\right]_{T_0}. \quad (15)$$

Equation (15) lays out the complexity of $V_{\rm oc}(T)$ when nonlinear behavior is observed. The second term is the reduction of the activation energy due to band tails. The third term is expected to be negative based on Eq. (14). The ideality factor variation with temperature depends on the underlying mechanism, but generally $dA/dT < 0$, being close to zero at room temperature and becoming increasingly negative as temperature decreases. At lower temperatures, trap-assisted tunneling mechanisms can lead to $A \propto 1/T$ [64,65] and nearly temperature-independent $V_{\rm oc}$, as observed in Fig. 2 above. The last term can be positive or negative depending on the T dependence of the logarithmic terms. For example, J_{00} can depend inversely proportionally to hole density, which is thermally activated, thereby making the last term negative.

It has been shown that the back-contact barrier can also cause $V_{\rm oc}(T)$ nonlinearity as temperature decreases [42,66,67]. We tested that for our case by simulating JV data down to $T = 200$ K using the same parameters as the black curve in Fig. 9, including the back barrier of 0.4 eV. Results are provided in the Supplemental Material [50]. In the simulations (Fig. S14), the curvature of $V_{\rm oc}(T)$ occurred for $T < 250$ K, while it was observed in the data for $T < 300$ K (see points in Fig. 4). Therefore, the back barrier may be affecting the $V_{\rm oc}(T)$ nonlinearity, but it is certainly not the primary cause.

Broadly though, any of the T dependence in Eq. (15) can lead to the observed nonlinearity in $V_{\rm oc}(T)$ as temperature decreases (cf. Fig. 2). The extended linear portion of $V_{\rm oc}(T)$ at $T \geq 300$ K from which we extracted E_a for a given light intensity is likely more representative of the physical activation energy than E_a extracted from lower temperatures because the T-dependent terms in Eq. (15) tend to diminish at higher temperature. A detailed study of the nonlinearity is beyond the present scope. Further discussion of factors that influence this analysis are presented in Refs. [26,28,29,68].

C. Light dependence of activation energy

As observed previously [30], the light-intensity dependence of E_a evident in Fig. 2 may be due to a transition from interface to bulk recombination with decreasing intensity, such that the activation energy increases from $E_{g,i}$ to E_g. We noted a similar trend in our simulation parameter space in the region of low bulk lifetime $\tau < 10$ ns and $S_f < 10^3$ cm/s, as shown in Fig. 3. However, the data for activation energy versus light intensity are quite different than the simulated results; the data indicate that E_a decreases more rapidly with light intensity than predicted by the model. From Fig. 2, the trend suggests eventual saturation at a lower limit of $E_a \approx 0.8$ eV as light intensity increases. It is plausible that the activation energy is light-sensitive due to defect occupation and photoinduced effects that can alter the conduction-band offset [69–71] and affect tunneling transport. Including *light-biased* photoemission spectroscopy, with the nondisruptive cleaving techniques presented herein, would help to elucidate the light dependence of the heterointerface band alignment [52].

We note that diode analysis to study $V_{\rm oc}(T)$ and determine E_a based on dark JV measurements should be approached with caution because E_a, and therefore J_0, can be very light-sensitive, as shown in Fig. 2.

D. Semiquantitative nature of the results

The obtained key values that govern recombination are inherently rough estimates. In particular, the value of S_f is very sensitive to ΔE_c. The fitting error of ± 0.036 eV for ΔE_c leads to a range of S_f that provides the same observed $V_{\rm oc} = 744$ mV. For the scenarios of Figs. 3 and 4, $S_f =$ 300–5000 cm/s provides the same $V_{\rm oc}$ over the ΔE_c range of -0.236 to -0.164 eV, as shown in Fig. 11. Additional uncertainty can arise from extraction of the effective band gap from QE, which can be affected by band-gap depth grading, especially for steep gradients [72,73].

We showed that QE is affected by the bulk lifetime value τ, but it also depends on the carrier mobility, μ, through

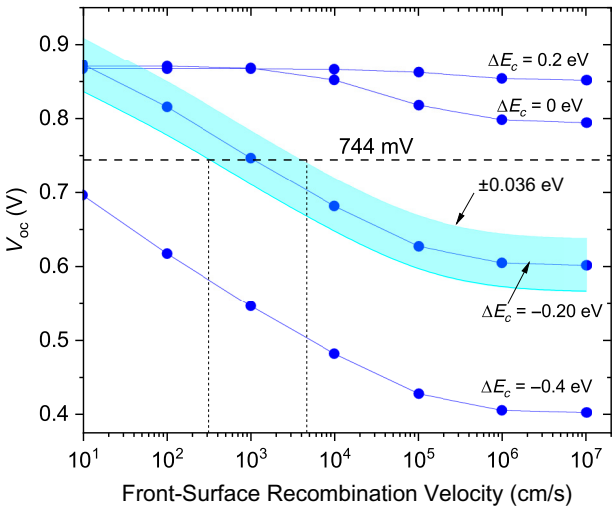

FIG. 11. Plot of $V_{\rm oc}$ versus front-surface recombination velocity for various conduction-band offsets, ΔE_c. The shaded region indicates ΔE_c uncertainty. The dashed line is $V_{\rm oc} = 0.744$ V. Model parameters are the same as those from Figs. 3 and 4.

the diffusion length, $L = \sqrt{\mu\tau kT/q}$. Accurate mobility measurement in thin-film photovoltaics is challenging. Reported measurements include $\mu = 85$–$100\ \mathrm{cm^2/(V\ s)}$ in undoped, large-grained polycrystalline $CdSe_{0.2}Te_{0.8}$ [74], 800 $\mathrm{cm^2/(V\ s)}$ in Cl-compensated single-crystal CdTe, and 10–100 $\mathrm{cm^2/(V\ s)}$ in As-doped single crystals with low dopant activation [75]. A minority-carrier mobility of $\mu_n < 100\ \mathrm{cm^2/(V\ s)}$ has been estimated in polycrystalline CdTe [76]. The simulations herein used $\mu_n = 40$ and $\mu_p = 10\ \mathrm{cm^2/(V\ s)}$, which are in the range of the latter measurements. The μ_n:μ_p ratio is from the common estimate of hole effective mass about four times greater than that of electrons in Cd(Se, Te) [77]. Given our $\tau = 5$ ns, the minority-carrier diffusion length is 720 nm, resulting in some collection loss over the 3-μm absorber depth.

With V_{oc} dominated by front-interface recombination, it is questionable whether bulk or back-interface recombination governs the shape of the QE curve at long wavelengths. Hence, QE was simulated for a range of $\tau =$ 5–1000 ns and $S_b = 10$–10^7 cm/s, with all other parameters as in the case study device (model 4T in Table I) and a back barrier of $\phi_{bp} = 0.4$ eV. The results shown in the Supplemental Material [50] indicate that minimizing bulk recombination ($\tau = 1000$ ns) and maximizing $S_b = 10^7$ cm/s does not account for the drop-off in QE with wavelength. For this device, carrier collection is relatively insensitive to S_b under short-circuit conditions.

Given that many of the parameters are coupled and uncertain, the method demonstrated here provides semiquantitative estimates, but important insights into the relative impacts of various V_{oc} loss mechanisms. It also provides guidance for where to focus attention for device improvements, which in this case is the front interface. Uniquely identifying V_{oc} loss pathways may be more challenging for high-efficiency devices. In such cases, the same approach can be used, but additional data may be required. For example, model parameters could be further constrained by light- and/or voltage-biased QE, additional intensity-dependent PL and TRPL, drive-level capacitance profiling, and improved mobility measurements. Finally, the scope of this work was to describe and demonstrate a multimode approach for evaluating V_{oc} losses, but a statistically representative number of samples should be studied in practice.

V. CONCLUSIONS

A combined multiple characterization and device simulation approach was employed to determine the primary sources of V_{oc} loss in a Cd(Se, Te) photovoltaic device. A summary of the calculated V_{oc} values for the cases considered herein is provided in Fig. 12. The case study device had $V_{oc} = 0.744$ V, significantly below the radiative limit of 1.146 V. Most of the losses occur at the front interface due to a clifflike conduction-band offset and interface recombination. Band tails with an exponential decay energy of 22 meV result in an additional loss of 40–70 mV. Alleviating front-interface effects alone can increase V_{oc} by about 100 mV. Further improvement would require increasing the bulk lifetime. Minimization of front-interface and bulk-recombination along with band-tail effects leads to $V_{oc} = 1$ V, at which point back-surface recombination becomes increasingly important. Nuances of this generally applicable approach were discussed.

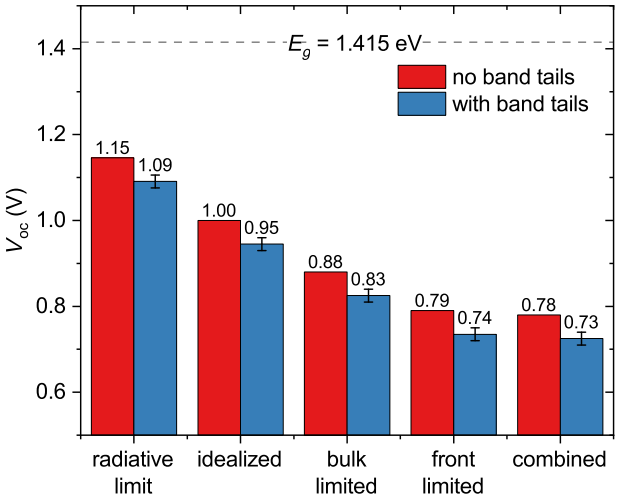

FIG. 12. Open-circuit voltage V_{oc} with and without band tails for the radiative limit case and the models in Table I. Band-tail losses are estimated at 55 mV with error bars of ±15 mV in each case. The combined model represents the device under study, with voltage losses almost entirely due to front-interface limitations.

VI. METHODS

A. Device fabrication

The superstrate TFPV device structure was fabricated at NREL, beginning with clean TEC12D (commercial glass coated with fluorine-doped SnO_2) that was coated in a two-step evaporation process with a 500-nm layer from an effusion cell loaded with $CdSe_{0.3}Te_{0.7}$ material (5N plus, −14/+60 mesh) followed by a 250-nm layer from an effusion cell loaded with CdTe material (5N plus, −14/+60 mesh) with the substrate held nominally at 450 °C. That was followed by growth of a 2-μm-thick CdTe:As layer grown by vapor transport deposition (VTD) from a mixed powder source of CdTe (5N plus, −100/+200 mesh) and Cd_3As_2 (Materion, −100 mesh). After deposition, a "densification anneal" at 575 °C with a CdTe overpressure was performed to mitigate voiding from rapid cooldown in the VTD. This is followed by a 60-min 450 °C $CdCl_2$ anneal that leads to diffusion of both the Se and As, resulting in a graded Se profile and redistribution of the As throughout the device. The $CdCl_2$ treatment is also known to enhance crystallite grain growth while passivating grain boundaries

and interfaces [78,79]. Prior to metallization, the back surface was prepared by rinsing the $CdCl_2$-treated sample in deionized water, then annealing in static air at 210 °C for 25 min. Evaporation was then used to deposit 100 nm of Au through a shadow mask, forming a 5×5 mm^2 device. The TCO layers were exposed and the cell was isolated using mechanical scraping. Finally, an indium busbar was soldered around the cell on the exposed TCO layers to finish the device.

Selenium variation produced a graded band gap between 1.4 and 1.5 eV, as measured by SIMS (see the Supplemental Material [50]). Arsenic was more evenly distributed with depth, except for significant accumulation near the Cd(Se, Te)/SnO_2 interface. Capacitance-voltage measurements indicated acceptor doping of approximately 2×10^{16} cm^{-3} (see Supplemental Material [50] for data). Comparing the latter to the integrated SIMS measurements of As suggests an averaged dopant activation of 2%; such low activation is an ongoing area of research for Cd(Se, Te) absorbers [80–82].

B. Characterization

JVTi data are collected using a current-voltage source and meter (Agilent B2912A) connected to the sample contacts in a two-wire configuration when the sample is mounted in a closed-cycle helium cryostat. Even though absolute currents are small, there may be some series resistance effects. Temperature is swept through the desired range using a temperature controller (Lakeshore 331) that stabilizes the sample temperature to within one degree Celsius. An automated data collection program is set to maintain the stabilized temperature for a designated time (1–5 min) before the current-voltage data are collected. Since conductive cooling and heating through the glass leads to temperature offsets between the cold-finger stage and the sample, the device temperature is recorded using a second sensor that is attached directly to the device side of the glass substrate. The sample is illuminated through the cryostat windows and a hole in the cold-finger stage with a Xe-bulb-based solar simulator capable of greater than 1-sun intensity. Multiple intensity levels of the solar-simulated light can be selected with automated neutral-density filters.

For photoelectron spectroscopy (PES) measurements, devices were mounted for thermomechanical cleaving, cleaved in an argon atmosphere, and transferred to the photoemission system without air exposure. XPS and UPS data were taken on a customized Physical Electronics VersaProbe III using monochromatic Al $K\alpha$ radiation for XPS and light from a polychromatic windowless helium lamp for UPS. High-energy-resolution spectra were taken at a pass energy of 27 eV and at normal exit angle. The binding-energy scale was calibrated at low binding energy using the Fermi-edge feature of cleaned metal foils, and at higher binding energy using the copper $2p_{3/2}$ photoelectron line. Satellites in UPS spectra were removed numerically. Low-energy inverse photoemission data were energy-calibrated using the Fermi-edge feature of clean silver foil.

A Newport-Oriel IQE-200 system was used to take external quantum efficiency measurements over a wavelength range of 300–1000 nm with a 10-nm step size and lock-in frequency of 37 Hz. PL was measured with 632.8-nm wavelength excitation using 1.98×10^{21} photons/(m^2 s) fluence. Absolute calibration was from comparison with a 2% reflectance standard. To increase PL signal-to-noise ratio, for the relatively weakly emitting sample, an interface cleaving technique was used [52]. The PL setup was calibrated for spectral sensitivity using manufacturer-provided traceable quartz tungsten halogen light calibration sources (Intellical, Princeton Instruments) [83]. Absolute photon numbers were obtained by using reflectance standards (LabSphere). TRPL with excitation at 405 and 670 nm was used to generate carriers with different initial distributions, as described in the Supplemental Material [50].

C. Numerical modeling

Device simulations were based on solving the Poisson and current continuity equations with the finite-element method using COMSOL Multiphysics® software. Simulations of JVTi, QE, and TRPL were conducted. JVTi studies included temperature dependencies of the carrier densities given by Fermi-Dirac statistics, mobility, and effective densities of states of the valence and conduction bands. Light intensity was controlled by evenly scaling the AM1.5G spectrum relative to 1 sun = 100 mW/cm^2. To account for band-gap grading, a depth-dependent absorption coefficient was used in the Cd(Se, Te) layer, $\alpha(E, x) = A\sqrt{E - E_g(x)}$, where $A = 10^5$ cm^{-1} eV$^{-1/2}$ and $E \geq E_g$ is photon energy. The absorption coefficient was replaced by Eq. (6) for cases with band tails. Both the absorber E_g and electron affinity varied with depth, depending on the Se grading, according to bowing parameters [55]. Parameter values and temperature dependencies are provided in the Supplemental Material [50]. For TRPL simulations, the time-dependent versions of the equations were solved with laser pulse excitation centered at 3 ps and a FWHM of 0.35 ps. Further details and parameter values, largely based on Refs. [8,77], are provided in the Supplemental Material [50].

ACKNOWLEDGMENTS

This work was authored in part by the National Renewable Energy Laboratory, operated by Alliance for Sustainable Energy, LLC, for the U.S. Department of Energy (DOE) under Contract No. DE-AC36-08GO28308. Funding was provided by the U.S. Department of Energy, Office

of Energy Efficiency and Renewable Energy, Solar Energy Technologies Office under agreement 38257. The views expressed in the article do not necessarily represent the views of the DOE or the U.S. Government. The U.S. Government retains and the publisher, by accepting the article for publication, acknowledges that the U.S. Government retains a nonexclusive, paid-up, irrevocable, worldwide license to publish or reproduce the published form of this work, or allow others to do so, for U.S. Government purposes.

[1] NREL. Best research-cell efficiency chart, https://www.nrel.gov/pv/cell-efficiency.html (accessed 2024-03-10).

[2] F. Xu, M. Zhang, Z. Li, X. Yang, and R. Zhu, Challenges and perspectives toward future wide-bandgap mixed-halide perovskite photovoltaics, Adv. Energy Mater. **13**, 2203911 (2023).

[3] R. Scaffidi, G. Birant, G. Brammertz, J. de Wild, D. Flandre, and B. Vermang, Ge-alloyed kesterite thin-film solar cells: Previous investigations and current status – A comprehensive review, J. Mater. Chem. A **11**, 13174 (2023).

[4] R. Gutzler, W. Witte, A. Kanevce, D. Hariskos, and S. Paetel, V_{oc}-losses across the band gap: Insights from a high-throughput inline process for CIGS solar cells, Prog. Photovolt.: Res. Appl. **31**, 1023 (2023).

[5] M. A. Scarpulla, *et al.*, CdTe-based thin film photovoltaics: Recent advances, current challenges and future prospects, Sol. Energy Mater. Sol. Cells **255**, 112289 (2023).

[6] A. Onno, C. Reich, S. Li, A. Danielson, W. Weigand, A. Bothwell, S. Grover, J. Bailey, G. Xiong, and D. Kuciauskas, Understanding what limits the voltage of polycrystalline CdSeTe solar cells, Nat. Energy **7**, 400 (2022).

[7] S. Rühle, Tabulated values of the Shockley–Queisser limit for single junction solar cells, Sol. Energy **130**, 139 (2016).

[8] A. Kanevce, M. O. Reese, T. M. Barnes, S. A. Jensen, and W. K. Metzger, The roles of carrier concentration and interface, bulk, and grain-boundary recombination for 25% efficient CdTe solar cells, J. Appl. Phys. **121**, 214506 (2017).

[9] P. Gorai, D. Krasikov, S. Grover, G. Xiong, W. K. Metzger, and V. Stevanović, A search for new back contacts for CdTe solar cells, Sci. Adv. **9**, eade3761 (2023).

[10] A. Danielson, C. Reich, R. Pandey, A. Munshi, A. Onno, W. Weigand, D. Kuciauskas, S. Li, A. Bothwell, and J. Guo, Electro-optical characterization of arsenic-doped CdSeTe and CdTe solar cell absorbers doped in-situ during close space sublimation, Sol. Energy Mater. Sol. Cells **251**, 112110 (2023).

[11] V. G. Karpov, A. D. Compaan, and D. Shvydka, Effects of nonuniformity in thin-film photovoltaics, Appl. Phys. Lett. **80**, 4256 (2002).

[12] V. G. Karpov, A. D. Compaan, and D. Shvydka, Random diode arrays and mesoscale physics of large-area semiconductor devices, Phys. Rev. B **69**, 045325 (2004).

[13] F. Urbach, The long-wavelength edge of photographic sensitivity and of the electronic absorption of solids, Phys. Rev. **92**, 1324 (1953).

[14] J. Jean, T. S. Mahony, D. Bozyigit, M. Sponseller, J. Holovský, M. G. Bawendi, and V. Bulović, Radiative efficiency limit with band tailing exceeds 30% for quantum dot solar cells, ACS Energy Lett. **2**, 2616 (2017).

[15] J. Wong, S. T. Omelchenko, and H. A. Atwater, Impact of semiconductor band tails and band filling on photovoltaic efficiency limits, ACS Energy Lett. **6**, 52 (2021).

[16] T. Gokmen, O. Gunawan, and D. B. Mitzi, Semi-empirical device model for $Cu_2ZnSn(S,Se)_4$ solar cells, Appl. Phys. Lett. **105**, 033903 (2014).

[17] J. E. Moore, C. J. Hages, R. Agrawal, M. S. Lundstrom, and J. L. Gray, The importance of band tail recombination on current collection and open-circuit voltage in CZTSSe solar cells, Appl. Phys. Lett. **109**, 021102 (2016).

[18] M. H. Wolter, R. Carron, E. Avancini, B. Bissig, T. P. Weiss, S. Nishiwaki, T. Feurer, S. Buecheler, P. Jackson, W. Witte, and S. Siebentritt, How band tail recombination influences the open-circuit voltage of solar cells, Prog. Photovolt.: Res. Appl. **30**, 702 (2022).

[19] J. K. Katahara and H. W. Hillhouse, Quasi-Fermi level splitting and sub-bandgap absorptivity from semiconductor photoluminescence, J. Appl. Phys. **116**, 173504 (2014).

[20] T. Song, A. Kanevce, and J. R. Sites, Emitter/absorber interface of CdTe solar cells, J. Appl. Phys. **119**, 233104 (2016).

[21] X. Fang, S. Ren, C. Li, C. Li, G. Chen, H. Lai, J. Zhang, and L. Wu, Investigation of recombination mechanisms of CdTe solar cells with different buffer layers, Sol. Energy Mater. Sol. Cells **188**, 93 (2018).

[22] L. Kujovic, X. Liu, A. Abbas, L. O. Jones, A. M. Law, M. Togay, K. M. Curson, K. L. Barth, J. W. Bowers, J. M. Walls, O. Oklobia, D. A. Lamb, S. J. C. Irvine, W. Zhang, C. Lee, T. Nagle, D. Lu, and G. Xiong, Achieving 21.4% efficient CdSeTe/CdTe solar cells using highly resistive intrinsic ZnO buffer layers, Adv. Funct. Mater. **34**, 2312528 (2024).

[23] M. Togay, R. C. Greenhalgh, T. A. Fiducia, T. Shimpi, W. Sampath, K. L. Barth, J. M. Walls, and J. W. Bowers, Transient metastable behavior caused by magnesium-doped zinc oxide emitters in CdSeTe/CdTe solar cells, IEEE J. Photovolt. **13**, 391 (2023).

[24] C. H. Swartz, S. R. Rab, S. Paul, M. F. A. M. van Hest, B. Dou, J. M. Luther, G. F. Pach, C. R. Grice, D. Li, S. S. Bista, E. G. LeBlanc, M. O. Reese, M. W. Holtz, T. H. Myers, Y. Yan, and J. V. Li, Measurement of band offsets and shunt resistance in CdTe solar cells through temperature and intensity dependence of open circuit voltage and photoluminescence, Sol. Energy **189**, 389 (2019).

[25] S. Paul, C. Swartz, S. Sohal, C. Grice, S. S. Bista, D.-B. Li, Y. Yan, M. Holtz, and J. V. Li, Buffer/absorber interface recombination reduction and improvement of back-contact barrier height in CdTe solar cells, Thin Solid Films **685**, 385 (2019).

[26] C. J. Hages, N. J. Carter, R. Agrawal, and T. Unold, Generalized current-voltage analysis and efficiency limitations in non-ideal solar cells: Case of $Cu_2ZnSn(S_xSe_{1-x})_4$ and $Cu_2Zn(Sn_yGe_{1-y})(S_xSe_{1-x})_4$, J. Appl. Phys. **115**, 234504 (2014).

[27] S. M. Sze, Y. Li, and K. K. Ng, *Physics of Semiconductor Devices* (John Wiley & Sons, Hoboken, NJ, 2021).

[28] S. Grover, J. V. Li, D. L. Young, P. Stradins, and H. M. Branz, Reformulation of solar cell physics to facilitate experimental separation of recombination pathways, Appl. Phys. Lett. **103**, 093502 (2013).

[29] J. V. Li, S. Grover, M. A. Contreras, K. Ramanathan, D. Kuciauskas, and R. Noufi, A recombination analysis of $Cu(In, Ga)Se_2$ solar cells with low and high Ga compositions, Sol. Energy Mater. Sol. Cells **124**, 143 (2014).

[30] R. E. Brandt, N. M. Mangan, J. V. Li, Y. S. Lee, and T. Buonassisi, Determining interface properties limiting open-circuit voltage in heterojunction solar cells, J. Appl. Phys. **121**, 185301 (2017).

[31] R. Scheer, Activation energy of heterojunction diode currents in the limit of interface recombination, J. Appl. Phys. **105**, 104505 (2009).

[32] M. Eron and A. Rothwarf, Effects of a voltage-dependent light-generated current on solar cell measurements: $CuInSe_2/Cd(Zn)S$, Appl. Phys. Lett. **44**, 131 (1984).

[33] Y. P. Varshni, Temperature dependence of the energy gap in semiconductors, Physica **34**, 149 (1967).

[34] R. Passler, Basic model relations for temperature dependencies of fundamental energy gaps in semiconductors, Phys. Status Solidi B **200**, 155 (1997).

[35] G. Fonthal, L. Tirado-Mejıa, J. I. Marın-Hurtado, H. Ariza-Calderon, and J. G. Mendoza-Alvarez, Temperature dependence of the band gap energy of crystalline CdTe, J. Phys. Chem. Solids **61**, 579 (2000).

[36] U. Rau and J. H. Werner, Radiative efficiency limits of solar cells with lateral band-gap fluctuations, Appl. Phys. Lett. **84**, 3735 (2004).

[37] J. Mattheis, U. Rau, and J. H. Werner, Light absorption and emission in semiconductors with band gap fluctuations – A study on $Cu(In, Ga)Se_2$ thin films, J. Appl. Phys. **101**, 113519 (2007).

[38] D. Abou-Ras, Microscopic origins of radiative performance losses in thin-film solar cells at the example of $(Ag, Cu)(In, Ga)Se_2$ devices, J. Vac. Sci. Technol., A **42**, 022803 (2024).

[39] A. P. Levanyuk and V. V. Osipov, Edge luminescence of direct-gap semiconductors, Sov. Phys. Usp. **24**, 187 (1981).

[40] B. I. Shklovskii and A. L. Efros, *Electronic Properties of Doped Semiconductors* (Springer Science & Business Media, Berlin, Heidelberg, 1984), Vol. 45.

[41] T. Gokmen, O. Gunawan, T. K. Todorov, and D. B. Mitzi, Band tailing and efficiency limitation in kesterite solar cells, Appl. Phys. Lett. **103**, 103506 (2013).

[42] N. Rosenblatt, J. Hack, C. Lee, Y.-H. Zhang, and W. K. Metzger, Impacts of band edge fluctuations on CdSeTe solar cell performance and models, APL Mater. **12**, 111117 (2024).

[43] E. O. Kane, Thomas-Fermi approach to impure semiconductor band structure, Phys. Rev. **131**, 79 (1963).

[44] R. Bhattacharya, B. Pal, and B. Bansal, On conversion of luminescence into absorption and the van Roosbroeck-Shockley relation, Appl. Phys. Lett. **100**, 222103 (2012).

[45] G. Rey, C. Spindler, F. Babbe, W. Rachad, S. Siebentritt, M. Nuys, R. Carius, S. Li, and C. Platzer-Björkman, Absorption coefficient of a semiconductor thin film from photoluminescence, Phys. Rev. Appl. **9**, 064008 (2018).

[46] E. M. Spaans, J. de Wild, T. J. Savenije, and B. Vermang, Unified potential fluctuations model for photoluminescence spectra at room temperature – $Cu(In, Ga)Se_2$ thin films, J. Appl. Phys. **130**, 123103 (2021).

[47] P. Wurfel, The chemical potential of radiation, J. Phys. C: Solid State Phys. **15**, 3967 (1982).

[48] G. Rey, G. Larramona, S. Bourdais, C. Choné, B. Delatouche, A. Jacob, G. Dennler, and S. Siebentritt, On the origin of band-tails in kesterite, Sol. Energy Mater. Sol. Cells **179**, 142 (2018).

[49] U. Rau, B. Blank, T. C. Müller, and T. Kirchartz, Efficiency potential of photovoltaic materials and devices unveiled by detailed-balance analysis, Phys. Rev. Appl. **7**, 044016 (2017).

[50] See Supplemental Material at http://link.aps.org/supplemental/10.1103/PhysRevApplied.23.034019 for (i) SIMS data, (ii) device model details, (iii) TRPL and QE data and simulations, (iv) PL fitting, (v) PES data, (vi) PL models with $\theta = 2$, (vii) $V_{oc}(T)$ with back barrier, and (viii) *C-V* data.

[51] A. Redinger, S. Kretzschmar, and T. Unold, in *2016 IEEE 43rd Photovoltaic Specialists Conference (PVSC)* (IEEE, Portland, OR, 2016), p. 3559.

[52] D. L. McGott, C. L. Perkins, and M. O. Reese, Thermomechanical cleave of polycrystalline CdTe solar cells and its applications: A review, Solar RRL **7**, 2300074 (2023).

[53] C. L. Perkins, C. Beall, M. O. Reese, and T. M. Barnes, Two-dimensional cadmium chloride nanosheets in cadmium telluride solar cells, ACS Appl. Mater. Interfaces **9**, 20561 (2017).

[54] J. Endres, D. A. Egger, M. Kulbak, R. A. Kerner, L. Zhao, S. H. Silver, G. Hodes, B. P. Rand, D. Cahen, L. Kronik, and A. Kahn, Valence and conduction band densities of states of metal halide perovskites: A combined experimental–theoretical study, J. Phys. Chem. Lett. **7**, 2722 (2016).

[55] J. Yang and S.-H. Wei, First-principles study of the band gap tuning and doping control in $CdSe_xTe_{1-x}$ alloy for high efficiency solar cell, Chin. Phys. B **28**, 086106 (2019).

[56] E. A. Kraut, R. W. Grant, J. R. Waldrop, and S. P. Kowalczyk, Precise determination of the valence-band edge in x-ray photoemission spectra: Application to measurement of semiconductor interface potentials, Phys. Rev. Lett. **44**, 1620 (1980).

[57] D. P. Shoemaker, C. W. Garland, and J. I. Steinfeld, *Experiments in Physical Chemistry* (McGraw-Hill, New York, NY, 2018).

[58] M. Maiberg, C.-Y. Song, M. Morawski, F. Neduck, H. Kempa, J. Damm, D. Hariskos, W. Witte, and R. Scheer, Toward digital twins by one-dimensional simulation of thin-film solar cells: $Cu(In, Ga)Se_2$ as an example, Phys. Rev. Appl. **21**, 034051 (2024).

[59] S. Siebentritt, U. Rau, S. Gharabeiki, T. P. Weiss, A. Prot, T. Wang, D. Adeleye, M. Drahem, and A. Singh, Photoluminescence assessment of materials for solar cell absorbers, Faraday Discuss. **239**, 112 (2022).

[60] J. H. Werner and H. H. Güttler, Barrier inhomogeneities at Schottky contacts, J. Appl. Phys. **69**, 1522 (1991).

[61] J. H. Werner, J. Mattheis, and U. Rau, Efficiency limitations of polycrystalline thin film solar cells: Case of Cu(In, Ga)Se_2, Thin Solid Films **480**, 399 (2005).
[62] L. V. Keldysh, The effect of a strong electric field on the optical properties of insulating crystals, Sov. Phys. JETP **7**, 788 (1958).
[63] J. Moseley, S. Grover, D. Lu, G. Xiong, H. L. Guthrey, M. M. Al-Jassim, and W. K. Metzger, Impact of dopant-induced optoelectronic tails on open-circuit voltage in arsenic-doped Cd(Se)Te solar cells, J. Appl. Phys. **128**, 103105 (2020).
[64] U. Rau, Tunneling-enhanced recombination in Cu(In, Ga)Se_2 heterojunction solar cells, Appl. Phys. Lett. **74**, 111 (1999).
[65] M. Nardone, V. G. Karpov, D. Shvydka, and M. L. C. Attygalle, Theory of electronic transport in noncrystalline junctions, J. Appl. Phys. **106**, 074503 (2009).
[66] T. Eisenbarth, R. Caballero, M. Nichterwitz, C. A. Kaufmann, H.-W. Schock, and T. Unold, Characterization of metastabilities in Cu(In, Ga)Se_2 thin-film solar cells by capacitance and current-voltage spectroscopy, J. Appl. Phys. **110**, 094506 (2011).
[67] T. Ott, F. Schönberger, T. Walter, D. Hariskos, O. Kiowski, O. Salomon, and R. Schäffler, Verification of phototransistor model for Cu(In, Ga)Se_2 solar cells, Thin Solid Films **582**, 392 (2015).
[68] R. E. Brandt, R. C. Kurchin, V. Steinmann, D. Kitchaev, C. Roat, S. Levcenco, G. Ceder, T. Unold, and T. Buonassisi, Rapid photovoltaic device characterization through Bayesian parameter estimation, Joule **1**, 843 (2017).
[69] W. R. Frensley and H. Kroemer, Theory of the energy-band lineup at an abrupt semiconductor heterojunction, Phys. Rev. B **16**, 2642 (1977).
[70] L. J. Brillson, *An Essential Guide to Electronic Material Surfaces and Interfaces* (Wiley Online Library, Sussex, UK, 2016).
[71] R. T. Tung and L. Kronik, Charge density and band offsets at heterovalent semiconductor interfaces, Adv. Theory Simul. **1**, 1700001 (2018).
[72] M. Troviano and K. Taretto, Analysis of internal quantum efficiency in double-graded bandgap solar cells including sub-bandgap absorption, Sol. Energy Mater. Sol. Cells **95**, 821 (2011).
[73] M. Richter, M. S. Hammer, T. Sonnet, and J. Parisi, Bandgap extraction from quantum efficiency spectra of Cu(In, Ga)Se_2 solar cells with varied grading profile and diffusion length, Thin Solid Films **633**, 213 (2017).
[74] D. Kuciauskas, J. Moseley, P. Ščajev, and D. Albin, Radiative efficiency and charge-carrier lifetimes and diffusion length in polycrystalline CdSeTe heterostructures, Phys. Status Solidi RRL **14**, 1900606 (2020).
[75] P. Ščajev, A. Mekys, L. Subačius, S. Stanionytė, D. Kuciauskas, K. G. Lynn, and S. K. Swain, Impact of dopant-induced band tails on optical spectra, charge carrier transport, and dynamics in single-crystal CdTe, Sci. Rep. **12**, 12851 (2022).
[76] D. Kuciauskas, A. Kanevce, J. N. Duenow, P. Dippo, M. Young, J. V. Li, D. H. Levi, and T. A. Gessert, Spectrally and time resolved photoluminescence analysis of the CdS/CdTe interface in thin-film photovoltaic solar cells, Appl. Phys. Lett. **102**, 173902 (2013).
[77] J. Moseley, D. Krasikov, C. Lee, and D. Kuciauskas, Diverse simulations of time-resolved photoluminescence in thin-film solar cells: A $SnO_2/CdSe_yTe_{1-y}$ case study, J. Appl. Phys. **130**, 163105 (2021).
[78] I. M. Dharmadasa, Review of the $CdCl_2$ treatment used in CdS/CdTe thin film solar cell development and new evidence towards improved understanding, Coatings **4**, 282 (2014).
[79] M. Amarasinghe, D. Albin, D. Kuciauskas, J. Moseley, C. L. Perkins, and W. K. Metzger, Mechanisms for long carrier lifetime in Cd(Se, Te) double heterostructures, Appl. Phys. Lett. **118**, 211102 (2021).
[80] T. Ablekim, E. Colegrove, and W. K. Metzger, Interface engineering for 25% CdTe solar cells, ACS Appl. Energy Mater. **1**, 5135 (2018).
[81] E. Colegrove, J. H. Yang, S. P. Harvey, M. R. Young, J. M. Burst, J. N. Duenow, D. S. Albin, S. H. Wei, and W. K. Metzger, Experimental and theoretical comparison of Sb, As, and P diffusion mechanisms and doping in CdTe, J. Phys. D: Appl. Phys. **51**, 075102 (2018).
[82] D. Krasikov and I. Sankin, Beyond thermodynamic defect models: A kinetic simulation of arsenic activation in CdTe, Phys. Rev. Mater. **2**, 103803 (2018).
[83] D. Kuciauskas, M. Nardone, A. Bothwell, D. Albin, C. Reich, C. Lee, and E. Colegrove, Why increased CdSeTe charge carrier lifetimes and radiative efficiencies did not result in voltage boost for CdTe solar cells, Adv. Energy Mater. **13**, 2301784 (2023).